



**HAL**  
open science

## Time-resolved imaging of OErsted field induced magnetization dynamics in cylindrical magnetic nanowires

M. Schöbitz, S. Finizio, A. de Riz, J. Hurst, C. Thirion, D. Gusakova, J. -C. Toussaint, J. Bachmann, J. Raabe, Olivier Fruchart

► **To cite this version:**

M. Schöbitz, S. Finizio, A. de Riz, J. Hurst, C. Thirion, et al.. Time-resolved imaging of OErsted field induced magnetization dynamics in cylindrical magnetic nanowires. *Applied Physics Letters*, 2021, 118 (17), pp.172411. 10.1063/5.0046643 . hal-03134319

**HAL Id: hal-03134319**

**<https://hal.science/hal-03134319v1>**

Submitted on 24 Aug 2023

**HAL** is a multi-disciplinary open access archive for the deposit and dissemination of scientific research documents, whether they are published or not. The documents may come from teaching and research institutions in France or abroad, or from public or private research centers.

L'archive ouverte pluridisciplinaire **HAL**, est destinée au dépôt et à la diffusion de documents scientifiques de niveau recherche, publiés ou non, émanant des établissements d'enseignement et de recherche français ou étrangers, des laboratoires publics ou privés.

# Time-resolved imaging of $\mathcal{O}$ ersted field induced magnetization dynamics in cylindrical magnetic nanowires

Cite as: Appl. Phys. Lett. **118**, 172411 (2021); doi: [10.1063/5.0046643](https://doi.org/10.1063/5.0046643)

Submitted: 5 February 2021 · Accepted: 31 March 2021 ·

Published Online: 28 April 2021



View Online



Export Citation



CrossMark

M. Schöbitz,<sup>1,2,3,a)</sup>  S. Finizio,<sup>4</sup>  A. De Riz,<sup>1</sup> J. Hurst,<sup>1</sup>  C. Thirion,<sup>3</sup> D. Gusakova,<sup>1</sup>  J.-C. Toussaint,<sup>3</sup>   
J. Bachmann,<sup>2,5</sup>  J. Raabe,<sup>4</sup>  and O. Fruchart<sup>1,a)</sup> 

## AFFILIATIONS

<sup>1</sup>Univ. Grenoble Alpes, CNRS, CEA, Spintec, 38054 Grenoble, France

<sup>2</sup>Friedrich-Alexander Univ. Erlangen-Nürnberg, Inorganic Chemistry, 91058 Erlangen, Germany

<sup>3</sup>Univ. Grenoble Alpes, CNRS, Institut Néel, 38042 Grenoble, France

<sup>4</sup>Swiss Light Source, Paul Scherrer Institut, 5232 Villigen PSI, Switzerland

<sup>5</sup>Institute of Chemistry, Saint-Petersburg State University, 198504 St. Petersburg, Russia

**Note:** This paper is part of the APL Special Collection on Mesoscopic Magnetic Systems: From Fundamental Properties to Devices.

**a)** Authors to whom correspondence should be addressed: [michael.schobitz@cea.fr](mailto:michael.schobitz@cea.fr) and [olivier.fruchart@cea.fr](mailto:olivier.fruchart@cea.fr)

## ABSTRACT

Recent studies in three-dimensional spintronics propose that the  $\mathcal{O}$ ersted field plays a significant role in cylindrical nanowires. However, there is no direct report on its impact on magnetic textures. Here, we use time-resolved scanning transmission x-ray microscopy to image the dynamic response of magnetization in cylindrical  $\text{Co}_{30}\text{Ni}_{70}$  nanowires subjected to nanosecond  $\mathcal{O}$ ersted field pulses. We observe the tilting of longitudinally magnetized domains toward the azimuthal  $\mathcal{O}$ ersted field direction and create a robust model to reproduce the differential magnetic contrasts and extract the angle of tilt. Furthermore, we report the compression and expansion, or breathing, of a Bloch-point domain wall that occurs when weak pulses with opposite signs are applied. We expect that this work lays the foundation for and provides an incentive to further studying complex and fascinating magnetization dynamics in nanowires, especially the predicted ultra-fast domain wall motion and associated spin wave emissions.

Published under license by AIP Publishing. <https://doi.org/10.1063/5.0046643>

Continuous developments in time-resolved magnetic imaging techniques have allowed for a shift of interest from systems that lend themselves more readily to imaging, such as flat nanostrips,<sup>1–3</sup> to more intricate systems such as three dimensional (3D) nanostructures, with added complexity from the volume.<sup>4,5</sup> Such 3D nanostructures can now be fabricated with increasing ease,<sup>6–8</sup> making the exploration of intriguing predicted magnetic configurations,<sup>9</sup> such as domain walls (DWs) in Möbius strips or hopfions,<sup>10</sup> feasible. A textbook case for such an investigation is provided by cylindrical magnetic nanowires (NWs), featuring a special type of DW, the Bloch-point wall (BPW),<sup>11</sup> which exhibits an azimuthal curling of magnetic moments around a Bloch point on the NW axis.<sup>12,13</sup> The dynamics of these walls are not yet well understood, but stand out compared to DWs in flat nanostrips due to fascinating theoretical predictions of fast, stable speeds,<sup>14</sup> accompanied by the controlled emission of spin waves.<sup>15</sup> Recent

experiments in NWs have shown that the  $\mathcal{O}$ ersted field induced by nanosecond current pulses plays a key role in stabilizing walls exclusively of the BPW type and, further, imposes an azimuthal circulation parallel to the field.<sup>16</sup> This allows controlling the wall structure and enables fast DW motion with speeds  $> 600$  m/s with the absence of Walker breakdown. The  $\mathcal{O}$ ersted field-induced BPW circulation switching was further studied in a simulation and theory work, revealing a complex mechanism of the switching process, involving nucleation and annihilation of pairs of vortex and anti-vortex.<sup>17</sup> Furthermore, magnetic moments in longitudinally magnetized domains are predicted to align azimuthally with the  $\mathcal{O}$ ersted field, with the degree of tilt related to a competition between magnetic exchange and Zeeman energy. Although some works have investigated the  $\mathcal{O}$ ersted field in nanowires,<sup>18–20</sup> its major influence on magnetization dynamics in these systems has become clear rather recently and is

especially pertinent in a low current density regime where the effect of spin-transfer torque is negligible.<sup>21</sup> However, few of the predictions have been confirmed experimentally.

Here, we make use of time-resolved scanning transmission x-ray microscopy (STXM) to image magnetization dynamics in NWs subjected to nanosecond pulses of  $\mathcal{E}$ sted field. Magnetically soft  $\text{Co}_{30}\text{Ni}_{70}$  NWs with diameters of 93, 97, and 101 nm were electrodeposited in anodized alumina templates and freed by dissolution of the template.<sup>6</sup> Wires were dispersed onto 200 nm thick,  $100 \times 100 \mu\text{m}^2$  wide x-ray transparent  $\text{Si}_3\text{N}_4$  windows, suspended in a  $5 \times 5 \text{mm}^2$  intrinsic Si frame. Individual wires were lithographically contacted with Au pads to allow for the injection of nanosecond pulses of electric current, in turn creating an  $\mathcal{E}$ sted field around the NW, as in Fig. 1(a). Magnetic images were acquired using STXM at the PoLux bending magnet beamline at the Swiss Light Source.<sup>22</sup> The sample was tilted by  $30^\circ$  with respect to the x-ray beam direction and aligned so that the NW was oriented to be as parallel as possible to the beam direction. Optical sensitivity to magnetization was achieved due to the x-ray magnetic circular dichroism (XMCD) effect, whereby circularly polarized x-ray light is absorbed differently depending on whether the magnetization is (anti-)parallel to the photon propagation direction. Magnetization dynamics were observed with time-resolved STXM as shown in Fig. 1(a), making use of the intrinsically pulsed nature of synchrotron radiation (purple) and phase locking their frequency with the excitation signal (i.e., current pulses in green).<sup>23</sup> Time-resolved image series composed of 1021 frames, each spaced by 200 ps, were

acquired stroboscopically with a temporal resolution of 70 ps and a spatial resolution of  $\approx 40 \text{ nm}$ . Each frame is an x-ray absorption spectroscopy (XAS) image acquired with circularly polarized light, with the magnetic contribution to intensity superimposed on the spectroscopy image. Differential magnetic contrast was revealed by a division of each XAS frame by the average of all XAS frames, with the latter essentially being a XAS image of the static magnetic state (full videos are given in the [supplementary material](#)).

To set ideas, consider the example of a time-resolved series with two frames where dynamics with opposite magnetic changes cause a variation in intensity of  $\pm I_D$ . The intensity in each frame is given as  $I_S \pm I_D$ , with  $I_S$  being the static contribution to the transmitted intensity. The average of the two frames is simply the static part,  $I_S$ , and thus, the differential magnetic contrast in each frame is given by

$$(I_S \pm I_D)/I_S = 1 \pm I_D/I_S. \quad (1)$$

While static XMCD contrast (usually of the order of a few percent) arises from the difference between XAS images taken with opposite polarizations of light, differential magnetic contrast is much weaker and of the order of 0.1%. It should be noted that if the dynamics do not lead to  $\pm I_D$  that is symmetric about zero, great care must be taken in the analysis, as discussed later on.

We first investigated the effect of the  $\mathcal{E}$ sted field on uniformly magnetized domains in  $\text{Co}_{30}\text{Ni}_{70}$  NWs. Suitable regions with  $>5 \mu\text{m}$ -long domains were detected using static XMCD STXM [Fig. 1(c)],

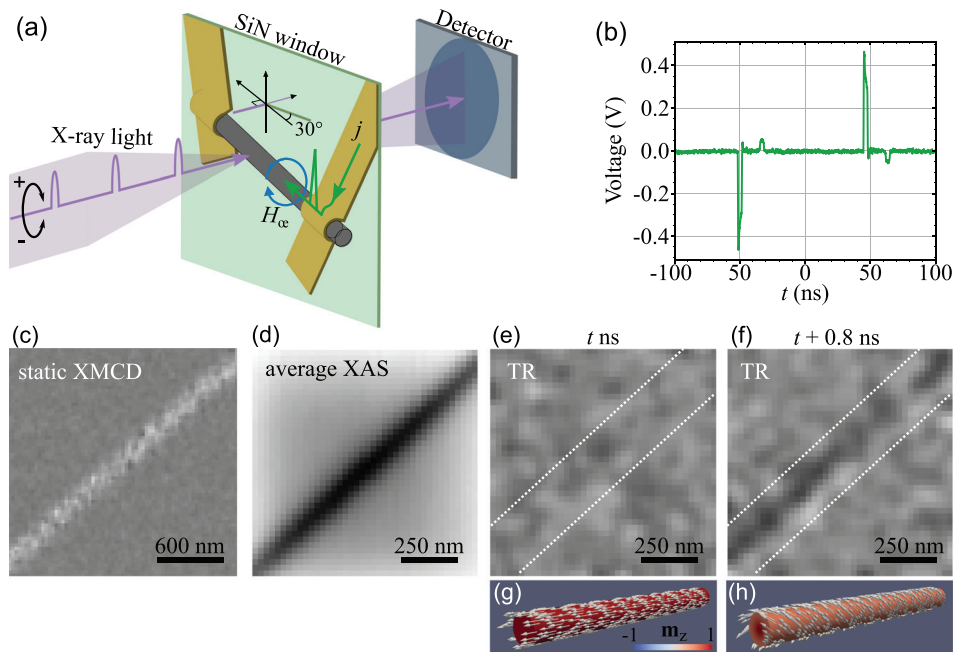


**FIG. 1.** Time-resolved STXM with electrically contacted magnetic NWs. (a) Schematic of the STXM set-up, with incoming circularly polarized x-ray photon bunches (purple) incident at  $30^\circ$  to the normal of the  $\text{SiN}$  window. In time-resolved mode, the frequency of the current pulses (green) inducing the  $\mathcal{E}$ sted field (blue) is phase-locked with the photon bunch frequency. (b) Voltage pulse signal measured after the NW across a  $50 \Omega$  load, with (+) and (−) pulses of 3 ns applied to induce a current density of  $j = 1.1 \times 10^{12} \text{ A/m}^2$  in a 93 nm diameter NW. (c) Static XMCD image of a longitudinal domain in a 93 nm diameter NW. (d) Average of all XAS frames in one time-resolved image series equivalent to  $I_S$  in Eq. (1). (e, f) Frames from a time-resolved image series showing the differential magnetic contrast observed in a 93 nm diameter  $\text{Co}_{30}\text{Ni}_{70}$  NW with the wire edges shown as guides to the eye. No current is flowing at time  $t$  (e), but at time  $t + 0.8 \text{ ns}$ , (f) the 3 ns current pulse with an amplitude of  $1.1 \times 10^{12} \text{ A/m}^2$  is being applied. (g, h) Illustrations of the magnetization in the NW at the time corresponding to frames [(e) and (f)].

after which a  $<1 \mu\text{m}$  section was chosen within this. A repeating signal of 3 ns alternating positive (+) and negative (−) voltage pulses with an amplitude of  $1.1 \times 10^{12} \text{A/m}^2$  was applied to a 93 nm diameter NW [Fig. 1(b)]. Pulses were spaced by 100 ns to allow for sufficient heat dissipation. The frames displayed in Figs. 1(e) and 1(f) show snapshots of the differential magnetic contrast observed before and during the application of the (+) current pulse. Before the application of current in Fig. 1(e), no contrast is observed since magnetization is at rest along the NW long axis [see the corresponding illustration in Fig. 1(g)] as it is for the majority of frames in the time-resolved series. During the application of the 3 ns (+) current pulse Fig. 1(f), a bipolar contrast is observed across the NW, indicating the tilting of magnetization to become more parallel (black) or antiparallel (white) to the x-ray beam direction. The wire magnetization is, thus, tilting toward the wire azimuthal direction [see the illustration in Fig. 1(h)], consistent with the direction of the  $\mathcal{C}$ ersted field. Once the pulse has ended, the magnetization returns to its relaxed state and the differential magnetic contrast is no longer observed. The second pulse, with opposite polarity, gives rise to an inverted contrast.

The signal-to-noise ratio is increased by taking the average of the 15 frames acquired during the 3 ns current pulse [Fig. 2(b)]. A width-averaged line scan across the wire [blue area in Fig. 2(b)] reveals the profile of this bipolar contrast [blue in Fig. 2(c)], with asymmetric peak amplitudes of 0.2% and −0.3%. This is expected to be a signature of the tilting of magnetization due to the  $\mathcal{C}$ ersted field, where appropriate fitting may extract quantitative information. In the following, we propose a model to reproduce this relatively simple physical situation and, hence, fit the recorded contrast profile to estimate the tilt angle.

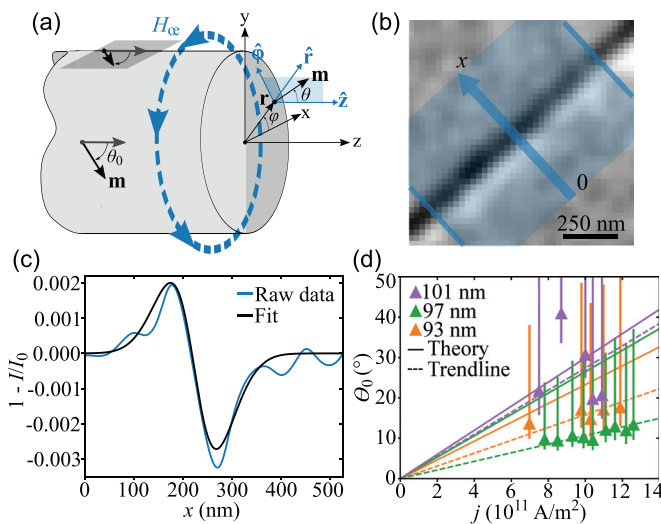


**FIG. 2.** Tilting of magnetization in NW domains as a function of current density. (a) Schematic of a NW with magnetic moment,  $\mathbf{m}$ , described by spherical polar angles  $\theta$  and  $\phi$  in the cylindrical coordinate system  $(r, \phi, z)$ . An applied  $\mathcal{C}$ ersted field tilts  $\mathbf{m}$  from  $\hat{z}$  toward  $\hat{\phi}$  by an angle,  $\theta$ . (b) Average differential magnetic contrast of all 15 frames acquired during the application of a 3 ns current pulse with an amplitude of  $1.1 \times 10^{12} \text{A/m}^2$  in a 93 nm diameter NW. The width-averaged line scan is indicated by the blue arrow. The corresponding intensity profile is shown in blue in (c). The black curve is the fit from our model, with  $\theta_0 = 18.9^\circ$ . (d)  $\theta_0$  as a function of applied current density,  $j$ , in three different NW samples with diameters 93, 97, and 101 nm and with vertical error bars. Trendlines through each data set and analytical solutions [see Eq. (4)] for each wire diameter are shown as dashed and solid lines, respectively.

Our model considers the radius-dependent degree of tilt within a NW cross section, the absorptivity of x-rays in the material, and the x-ray beam spot size, which make up the key components of magnetic transmission x-ray imaging.<sup>4</sup>

We use an Ansatz to describe the tilt by an angle  $\theta$  of magnetic moment,  $\mathbf{m}$ , toward the azimuthal direction when subjected to the  $\mathcal{C}$ ersted field [Fig. 2(a)],

$$\theta(r) = \theta_0 \sin\left(\frac{\pi r}{2R}\right). \quad (2)$$

$\mathbf{r}$  is any point within the circular wire cross section,  $r = |\mathbf{r}|$ ,  $R$  is the wire radius, and  $\theta_0 = \theta(r = R)$ . Comparisons with micromagnetic simulations showed that this Ansatz accurately describes the tilt within the wire.<sup>17</sup>

In magnetic materials, the absorptivity,  $\mu$ , or linear rate of absorption of x-rays depends on the chemical composition, the x-ray energy, and the magnetization direction vs the polarity of circularly polarized x-ray light. For a 100% circularly (+) or (−) polarized x-ray beam parallel to the magnetization, the absorptivity is given as  $\mu_{\pm}$  and we additionally define the average absorptivity,  $\mu_{\text{av}} = (\mu_{-} + \mu_{+})/2$ , and the difference in absorptivity,  $\Delta\mu = \mu_{-} - \mu_{+}$ . The amplitude of the latter is of particular importance, as it directly influences the strength of the XMCD effect and, thus, relates to the strength of any differential magnetic contrast. Values for  $\mu_{\text{av}}$  and  $\Delta\mu$  of the studied  $\text{Co}_{30}\text{Ni}_{70}$  NWs at the Co L3 absorption edge can be extracted from XAS images acquired with circularly polarized light in static STXM. The reduced x-ray intensity behind an NW is described by the Beer-Lambert law, linking the exponential decay of light intensity through matter with  $\mu$ . Intensity profiles taken across the NW can, thus, be fitted with the law; however, a non-zero x-ray spot size must be accounted for by a convolution with a Gaussian with width  $\sigma$ . A detailed analysis is shown in the [supplementary material](#). The fitting procedure then provides the only free parameters, absorptivity,  $\mu$ , and spot size,  $\sigma$ . The analysis relies on the  $30^\circ$  angle between the NW magnetization and the x-ray beam, induced by the sample holder orientation. It is also due to this angle that a geometrical adjustment must be made to calculate  $\Delta\mu$  from the extracted  $\mu$  (see the [supplementary material](#)).

Using this fitting procedure on multiple XAS images, we determined  $\mu_{\text{av}} = 0.006 \pm 0.002 \text{nm}^{-1}$  and also found an average of  $\sigma = 50 \pm 4 \text{nm}$ , where the uncertainty is the standard deviation of the data sets. For comparison, the theoretical absorptivity for  $\text{Co}_{30}\text{Ni}_{70}$  at the Co L3 edge is  $\mu_{\text{av,th}} = 0.019 \text{nm}^{-1}$ , which is a factor 3 larger than our extracted values.<sup>24</sup> This is a common feature in STXM imaging, partly related to background intensity incident on the x-ray detector. We expect that this background intensity amounts to  $\approx 33\%$  at the PolLux beamline STXM and arises from higher-order light from the monochromating mirror ( $\approx 15\%$ )<sup>25</sup> and leakage of the zone plate center stop ( $\approx 18\%$ ). Accounting for this via a subtraction from the static XAS images, we correct  $\mu_{\text{av}} = 0.011 \pm 0.005 \text{nm}^{-1}$ , which is closer to the theoretical value. The reason for the remaining difference is unclear. We similarly correct  $\Delta\mu$  from  $0.002 \pm 0.001 \text{nm}^{-1}$  to  $0.003 \pm 0.002 \text{nm}^{-1}$  (the uncertainty also being the standard deviation). Accounting for the  $\approx 50\%$  degree of circular polarization of x-ray light in this experiment, we find a  $\Delta\mu = 0.006 \pm 0.004 \text{nm}^{-1}$ . This can be compared to the theoretical value, which again for the Co L3 edge is  $\Delta\mu_{\text{th}} = 0.01 \text{nm}^{-1}$ .<sup>24</sup> Our calculated value is again lower than theory, but still in reasonable agreement considering the uncertainty.

The background subtraction was, therefore, applied to all acquired STXM images. It should be noted that considering the derived values of  $\mu_{av}$  and  $\Delta\mu$  as effective allows extracting the exact magnetization direction if the values were calibrated on uniform magnetization at  $30^\circ$ .

To now fit the bipolar contrast profile in Fig. 2(c), we reuse the Beer-Lambert law and include non-uniform magnetization, such as described by our Ansatz in (2),

$$I(x) = I_0 \exp - \int \left( \mu_{av} + \frac{1}{2} \Delta\mu \hat{\mathbf{k}} \cdot \mathbf{m} \right) d\ell. \quad (3)$$

This describes the progressive absorption of x-rays through each elementary segment with length,  $d\ell$ , and with  $\hat{\mathbf{k}} \cdot \mathbf{m}$ , the component of magnetization along the x-ray beam direction,  $\hat{\mathbf{k}}$ .  $I$  depends on  $\mathbf{m}(r)$ , which itself depends on  $\theta_0$ .

The intensity profile is then convoluted with the Gaussian to account for the finite spot size, already determined from the static XAS image analysis. By performing the same image calculation as in Eq. (1) with the dynamic ( $\theta_0 \neq 0$ ) and the static ( $\theta_0 = 0$ ) intensity profile, the bipolar differential magnetic contrast profiles can be reproduced. The only free parameter for the fit is  $\theta_0$ , while all other variables are fixed as previously determined from the XAS image analysis. We revisit now the magnetic image in Fig. 2(b) and the corresponding contrast profile in blue in Fig. 2(c), which is fit very well ( $r^2 = 0.94$ ) by the black curve. The model also reproduces the asymmetric signal, which originates in part from the non-linear change in  $\hat{\mathbf{k}} \cdot \mathbf{m}$  due to the geometry of the  $30^\circ$  sample holder and in part from the non-linear x-ray absorption due to the exponential nature of the Beer-Lambert law. From the fit, we determine the tilt of magnetic moments on the surface as  $\theta_0 = 18.9^\circ$ , caused by the current pulse-induced CErsted field. This value comes with multiple sources of uncertainty for the magnitude of the extracted  $\theta_0$ . First, we determined that the uncertainty in the NW diameter measured from scanning electron microscopy images and the uncertainty in the spot size extracted from the XAS analysis translate to an uncertainty of  $\leq 10\%$  in  $\theta_0$ . This remains moderate compared with the last source, the uncertainty in  $\mu_{av}$  and  $\Delta\mu$ , for which the impact is critical due to the aforementioned exponential in (3). We repeat the fitting of the data in Fig. 2(c) using values for  $\mu_{av}$  of 0.006 and  $0.016 \text{ nm}^{-1}$  and  $\Delta\mu$  of 0.001 and  $0.004 \text{ nm}^{-1}$ , which correspond to an uncertainty of one standard deviation (see the supplementary material, Fig. S5). This gives  $\theta_{0,\text{max}} = 47.8^\circ$  and  $\theta_{0,\text{min}} = 13.2^\circ$ , which is strongly asymmetric about  $\theta_0 = 18.9^\circ$  due to the exponential in Eq. (3). These values of  $\theta_{0,\text{max}}$  and  $\theta_{0,\text{min}}$ , hence, provide the range of uncertainties that we expect for our extracted value of  $\theta_0$ . However, for the case of the intensity profile produced with  $\theta_{0,\text{max}}$ , the fit to the data is quite poor ( $r^2 = 0.83$ ), indicating that the original fit with  $\theta_0 = 18.9^\circ$  is more appropriate.

This fitting analysis to determine  $\theta_0$  was applied to multiple time-resolved image series from three wire diameters and several applied current densities,  $j$ , with the results plotted in Fig. 2(d). The vertical error bars for each data point represent the range of uncertainties calculated as described above. The most significant result is that  $\theta_0$  increases linearly with  $j$ , as also shown by the dashed trendline (constrained to pass through the origin) for each data set. While the linear dependence of the 93 and 97 nm diameter wires is clear, the 101 nm diameter wire exhibits a larger spread. The reason most likely is a variation in the imaging conditions from one time-resolved series to

another (when settings were changed), resulting in a change in the incident x-ray intensity. This directly impacts the signal-to-noise ratio in the differential images and possibly the applied background subtraction, as the latter may not scale linearly with the incident light intensity. In both instances, the result would be a vertical offset (of unknown direction) of the data. Imaging conditions (settings) were kept constant during the acquisition of each of the other two sample data sets; however, they were adjusted between the samples. For any  $j$ ,  $\theta_0$  increases from the 97 to 93 to 101 nm diameter wire and using the trendline, we find a tilt rate in  $\theta_0$  equivalent to 10.7, 16.0, and  $27.4^\circ$  per  $10^{12} \text{ A/m}^2$ , respectively.

To compare the experimental  $\theta_0$ , we use an analytical model developed by De Riz *et al.*,<sup>17</sup> balancing the competition between exchange and Zeeman CErsted energies to describe  $\theta_0(j)$  in longitudinal domains in NWs. To first order, this reads

$$\theta_0 \approx \frac{1}{3.16} \frac{\mu_0 j M_s R^3}{\pi A}, \quad (4)$$

with  $\mu_0 = 4\pi \times 10^{-7}$  being the vacuum magnetic permeability,  $M_s$  the spontaneous magnetization of the material, and  $A$  the exchange stiffness. De Riz *et al.* found that for  $j < 3 \times 10^{12} \text{ A/m}^2$ , the model is an accurate description and matches well with simulations, meaning that it is appropriate to compare with the results presented here. Using magnetic parameters for  $\text{Co}_{30}\text{Ni}_{70}$  NWs [ $M_s = 0.77 \text{ MA/m}$  (Ref. 26) and  $A = 1.5 \times 10^{-11} \text{ J/m}$  (Ref. 27)], Eq. (4) is plotted as a solid line for each NW diameter in Fig. 2(d). The theory confirms the experimentally observed linear dependence of  $\theta_0$  on  $j$ ; however, it predicts larger tilt rates. These are  $\theta_0 = 23.4^\circ$ ,  $26.5^\circ$ , and  $29.9^\circ$  per  $10^{12} \text{ A/m}^2$  for 93, 97, and 101 nm diameter wires, respectively. Although there is  $\leq 55\%$  discrepancy between the theory and experiment, the results are promising as they indicate that the analysis is appropriate within its range of uncertainties. The experiment fails to reproduce the theoretically predicted  $1/R^3$  dependence; however, we expect this to be linked to systematic errors such as the changes in imaging conditions discussed previously. Furthermore, local inhomogeneities in the nanowire (e.g. small changes in the diameter or crystal grains) can also lead to a systematic offset of the data both along  $\theta_0$  or  $j$  which cannot be accounted for.

We now turn to the imaging of BPWs under the influence of the CErsted field in the same NWs. DW positions were determined using static XMCD, after which a current pulse of sufficient amplitude ( $j \approx 1 \times 10^{12} \text{ A/m}^2$ ) was sent through the NW to ensure a) the BPW DW type by transforming walls of the transverse-vortex kind to BPWs<sup>17</sup> and b) that the BPW is sufficiently pinned on an extrinsic pinning site to allow for a reproducible magnetization process over millions of pulses. Multiple time-resolved series were acquired while applying a similar voltage pulse signal as in Fig. 1b, with different  $j$  values around  $j_c$ , the critical current density expected for BPW circulation switching.<sup>16,17</sup>

We imaged a tail-to-tail BPW in a 101 nm diameter NW, first in the regime when  $j < j_c$  by applying a current density of  $\pm 7.5 \times 10^{11} \text{ A/m}^2$ . Figures 3(a)–3(d) show the frame average of the differential magnetic contrast frames acquired during Fig. 3(a) the application of the 3 ns (+) current pulse, Fig. 3(b) the first 100 ns rest period, Fig. 3(c) the 3 ns (–) current pulse, and Fig. 3(d) the second 100 ns rest period. All frames were filtered with a hat wavelet filter to improve the signal-to-noise ratio. In addition to the CErsted field tilting

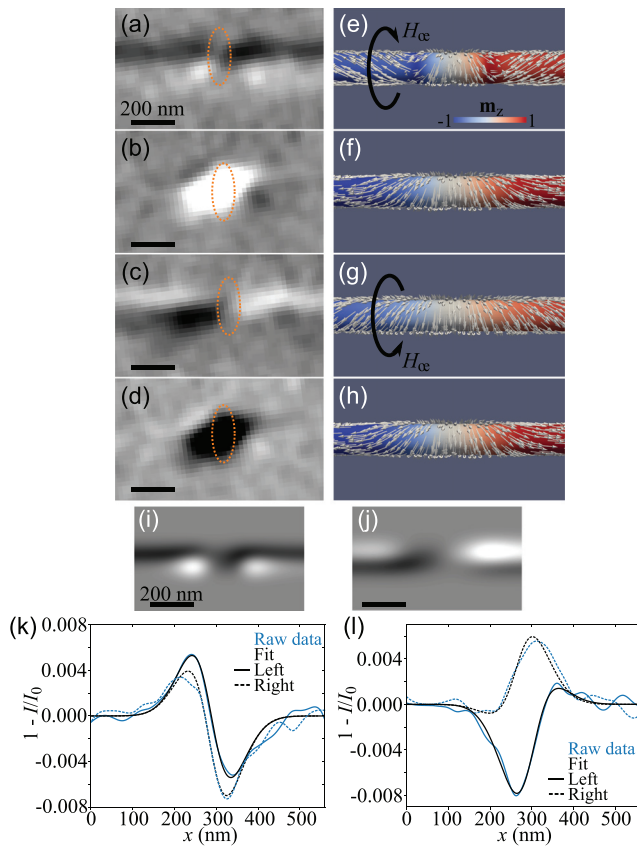


**FIG. 3.** BPW in a 101 nm diameter NW subjected to an Oersted field. Average of all wavelet filtered time-resolved differential magnetic contrast frames acquired during (a) the application of a 3 ns (+) current pulse with an amplitude of  $7.5 \times 10^{11}$  A/m<sup>2</sup>, (b) the 100 ns rest period, (c) the 3 ns (−) current pulse, and (d) the 100 ns rest period. The BPW position is indicated by orange circles. The micromagnetic simulations in (e–h) correspond to the images in (a)–(d) and show a tail-to-tail BPW in its compressed (a), expanded (g), and relaxed (f,h) state. The direction of the applied Oersted field is indicated where applicable. Simulated time-resolved differential magnetic contrast of a compressed (i) and expanded (j) BPW in a 100 nm diameter NW. Each frame was blurred with a Gaussian. Contrast profiles for the case of a compressed (k) and expanded (l) BPW, corresponding to line scans left (solid lines) and right (dashed lines) of the wall center. The true line scans from the image in (a) and (c) are shown in blue, while the fit from our model is shown in black.

observed within the domains during the pulse application, all four images contain a strong contrast at the BPW location (orange circle).

As expected for this regime, in Figs. 3(a) and 3(c), no specific differential magnetic contrast is visible at the wall center, indicating that the sign of azimuthal curling directly around the Bloch-point remains unchanged for the duration of the image series. The applied Oersted field pulses [see black arrows in Figs. 3(e) and 3(f)] are, thus, once parallel and once antiparallel to the wall circulation, so that different dynamics are expected during each of the two pulses. Indeed, in Figs. 3(a) and 3(c), we observe two different stronger contrasts around the wall center. In Fig. 3(a), there are four small symmetric lobes of differential magnetic contrast with a stronger intensity than that seen in the longitudinal domains far from the wall. The bipolar contrast to either

side of the wall center is indicative of a change in circulation that is now opposed to the static circulation (i.e., state  $I_S$ ), which can be understood as follows: the bipolar contrast, albeit stronger, matches that within the domains, suggesting a tilt toward the Oersted field direction. This tilt direction opposes the intrinsic BPW circulation, and as the BPW does not reverse its sign of circulation, the observed change, therefore, reflects rather a compression of the wall. Such a compression was predicted by micromagnetic simulations [Fig. 3(e)] of a tail-to-tail BPW in a 100 nm diameter Co<sub>30</sub>Ni<sub>70</sub> NW, subjected to an antiparallel Oersted field induced by a current with an amplitude of  $8 \times 10^{11}$  A/m<sup>2</sup>. These simulations were obtained using our homemade finite element freeware FEELLGOOD,<sup>28</sup> based on the Landau–Lifshitz–Gilbert equation. The simulated distribution of magnetization was further used to simulate XAS images<sup>29</sup> expected for an absorption according to Eq. (3) and governed by our experimentally determined values of  $\mu_{av}$  and  $\Delta\mu$ . Importantly, the 30° sample holder alignment was accounted for in the simulated imaging. Differential magnetic contrast images were calculated by applying Eq. (1) to simulated XAS images of a dynamic and static BPW. A Gaussian filter was applied to reproduce the effect of a finite width spot size as in the experiment (unfiltered images are shown in the supplementary material). The differential magnetic contrast simulated for a compressed tail-to-tail BPW is shown in Fig. 3(i). The similarity with the image in Fig. 3(a) is striking, thus confirming the qualitative explanation of a BPW compression. Minor differences, e.g., the size of certain features compared to in Fig. 3(a), are likely related to the Gaussian filter applied to the simulation.

Conversely, in Fig. 3(c), there are only two large lobes of opposite differential magnetic contrast, suggesting that the circulation of the static state is now being enhanced. This should be the result of an expansion of the BPW [see simulation in Fig. 3(g)] as the applied Oersted field is parallel to the wall circulation. The differential magnetic contrast from the simulated expanded wall Fig. 3(g) is shown in Fig. 3(j), with key contrast features again matching with those observed in Fig. 3(c). This combination between time-resolved imaging and simulated imaging provides a powerful tool to explain observed contrasts.

We now return to our model for a quantitative verification of the qualitative explanation. We plot in blue in Figs. 3(k) and 3(l) contrast profiles from line scans taken across the wire, through the regions of contrast left (solid curve) and right (dashed curve) of the BPW center. Figures 3(k) and 3(l) correspond to the images in Figs. 3(a) and 3(c), respectively. In this case, fitting is achieved because the static ( $I_S$ ) and the dynamic, either compressed or expanded, state intensity profiles are defined by separate  $\theta_0$  and are non-zero. It must be noted that the convolution with the Gaussian spot size along  $x$  only is now slightly less valid because the magnetization is no longer homogeneous along  $z$ , and a finer analysis should convolute along both the  $x$  and  $z$  direction. Still, the black curves in Figs. 3(k) and 3(l) are fits to the contrast profiles and show an excellent agreement on either side of the wall center. The BPW compression proposed to explain Fig. 3(a) is confirmed numerically with the fits in Fig. 3(k): left and right of the wall center,  $\theta_0$  tilts from 16° to −17° and from 28° to −8°, respectively. The Oersted field reverses the sign of circulation close to the wall center, compressing the wall and giving rise to the bipolar contrast and, hence, four contrast lobes around the wall center. Similarly, the fits for Fig. 3(i) reveal  $\theta_0$  tilts from 17° to 45° and from 20° to 41°, left and right of the wall center, respectively, confirming the enhancement of the static

circulation, or an expansion of the BPW. Figures 3(a) and 3(c) together show the breathing of the BPW, predicted only by simulations until now.<sup>17</sup> The differential magnetic contrast patterns were observed in multiple image series and are inverted in the case of a BPW with opposite static circulation (see the [supplementary material](#)).

For the interpulse periods displayed in Figs. 3(b) and 3(d), a strong white or black contrast, respectively, is observed at the DW location. This should be a result of small-scale BPW motion of the order of  $270 \pm 30$  nm; however, intricacies of this contrast, such as the direction of motion and a time evolution of the contrast, are not yet understood (see the [supplementary material](#) for further discussion).

We finally mention the case when  $j > j_c$ , for which the BPW switches its sense of circulation.<sup>16,17</sup> This could not be observed experimentally with time-resolved STXM because DWs disappeared for  $j \geq j_c$ , which we attribute to heat-assisted DW depinning. Future measurements, possibly with engineered DW pinning sites, are required to observe this effect with temporal resolution.

In conclusion, we have used time-resolved STXM to image dynamic changes of magnetic textures in cylindrical NWs. We observe the effect of the CErsted field on longitudinally magnetized domains and evidence the breathing of a BPW when subjected to pulses with opposite signs. A quantitative analysis of the differential magnetic contrast is provided by a robust model based on the absorptivity of x-rays and a description of the magnetization in a NW cross section. This highlights the depth of information obtainable by time-resolved magnetic imaging and that a direct comparison of the observed dynamics with simulations and theory is possible. Further work with this technique will significantly improve our understanding of magnetic 3D nanosized systems and enable better control over them.

See the [supplementary material](#) for the following: full time-resolved image series from which still frames are shown in this text (Figs. S1 and S2), calculation of the projection of magnetization in a tilted NW, detailed explanation of the XAS analysis and impact of the uncertainty in absorptivity on the asymmetric error bars on  $\theta_0$ , unfiltered simulated images of a breathing BPW, images of breathing of a BPW with switched circulation, and an explanation of differential magnetic contrast of BPW motion.

M.S. acknowledges a grant from the Laboratoire d'excellence LANEF in Grenoble (No. ANR-10-LABX-51-01). This project received financial support from the French National Research Agency (Grant No. JCJC MATEMAC-3D). This work was partly supported by the French RENATECH network and by the Nanofab platform (Institut Néel), whose team is greatly acknowledged for technical support. Part of the work was performed at the PolLux STXM endstation of the Swiss Light Source, Paul Scherrer Institut, Villigen PSI, Switzerland, financed by the German Bundesministerium für Bildung und Forschung (BMBF) through Contract Nos. 05K16WED and 05K19WE2.

## DATA AVAILABILITY

The data that support the findings of this study are available from the corresponding author upon reasonable request.

## REFERENCES

- K. Litzius, I. Lemesch, B. Krüger, P. Bassirian, L. Caretta, K. Richter, F. Büttner, K. Sato, O. A. Tretiakov, J. Förster, R. M. Reeve, M. Weigand, I. Bykova, H. Stoll, G. Schütz, G. S. D. Beach, and M. Kläui, *Nat. Phys.* **13**, 170 (2017).
- R. Juge, S.-G. Je, D. de Souza Chaves, L. D. Buda-Prejbeanu, J. Peña-García, J. Nath, I. M. Miron, K. G. Rana, L. Aballe, M. Foerster, F. Genuzio, T. O. Menteş, A. Locatelli, F. Maccherozzi, S. S. Dhesi, M. Belmeguenai, Y. Roussigné, S. Auffret, S. Pizzini, G. Gaudin, J. Vogel, and O. Boulle, *Phys. Rev. A* **12**, 044007 (2019).
- S. Finizio, S. Wintz, S. Mayr, A. J. Huxtable, M. Langer, J. Bailey, G. Burnell, C. H. Marrows, and J. Raabe, *Appl. Phys. Lett.* **117**, 212404 (2020).
- C. Donnelly and V. Scagnoli, *J. Phys.: Condens. Matter* **32**, 213001 (2020).
- C. Donnelly, S. Finizio, S. Gliga, M. Holler, A. Hrabec, M. Odstrčil, S. Mayr, V. Scagnoli, L. J. Heyderman, M. Guizar-Sicairos, and J. Raabe, *Nat. Nanotechnol.* **15**, 356 (2020).
- S. Bochmann, A. Fernandez-Pacheco, M. Mačkovič, A. Neff, K. R. Siefermann, E. Spiecker, R. P. Cowburn, and J. Bachmann, *RCS Adv.* **7**, 37627 (2017).
- G. Williams, M. Hunt, B. Boehm, A. Locatelli, T. O. Menteş, D. Ho, S. Giblin, D. Read, J. Rarity, R. Allenspach, and S. Ladak, *Nano Res.* **11**, 845 (2018).
- L. Skoric, D. Sanz-Hernández, F. Meng, C. Donnelly, S. Merino-Aceituno, and A. Fernández-Pacheco, *Nano Lett.* **20**, 184 (2020).
- A. Fernandez-Pacheco, R. Streubel, O. Fruchart, R. Hertel, P. Fischer, and R. P. Cowburn, *Nat. Commun.* **8**, 15756 (2017).
- S. Grytsiuk, J.-P. Hanke, M. Hoffmann, J. Bouaziz, O. Gomonay, G. Bihlmayer, S. Lounis, Y. Mokrousov, and S. Blügel, *Nat. Commun.* **11**, 511 (2020).
- S. Da Col, S. Jamet, N. Rougemaille, A. Locatelli, T. O. Menteş, B. S. Burgos, R. Afid, M. Darques, L. Cagnon, J. C. Toussaint, and O. Fruchart, *Phys. Rev. B* **89**, 180405 (2014).
- R. Feldtkeller, *Z. Angew. Phys.* **19**, 530 (1965).
- W. Döring, *J. Appl. Phys.* **39**, 1006 (1968).
- R. Wieser, E. Y. Vedmedenko, P. Weinberger, and R. Wiesendanger, *Phys. Rev. B* **82**, 144430 (2010).
- R. Hertel, *J. Phys.: Condens. Matter* **28**, 483002 (2016).
- M. Schöbitz, A. De Riz, S. Martin, S. Bochmann, C. Thirion, J. Vogel, M. Foerster, L. Aballe, T. O. Menteş, A. Locatelli, F. Genuzio, S. L. Denmat, L. Cagnon, J. Toussaint, D. Gusakova, J. Bachmann, and O. Fruchart, *Phys. Rev. Lett.* **123**, 217201 (2019).
- A. D. Riz, J. Hurst, M. Schöbitz, C. Thirion, J. Bachmann, J.-C. Toussaint, O. Fruchart, and D. Gusakova, *Phys. Rev. B* **103**, 054430 (2021).
- J. A. Otalora, D. Cortés-Ortuno, D. Görlitz, K. Nielsch, and P. Landeros, *J. Appl. Phys.* **117**, 173914 (2015).
- D. Aurelio, A. Giordano, L. Torres, G. Finocchio, and E. Martinez, *IEEE Trans. Magn.* **49**, 3211 (2013).
- J. A. Fernandez-Roldan, R. P. del Real, C. Bran, M. Vazquez, and O. Chubykalo-Fesenko, *Phys. Rev. B* **102**, 024421 (2020).
- J. Hurst, A. D. Riz, M. Staño, J.-C. Toussaint, O. Fruchart, and D. Gusakova, *Phys. Rev. B* **103**, 024434 (2021).
- J. Raabe, G. Tzvetkov, U. Flechsig, M. Böge, A. Jaggi, B. Sarafimov, M. G. C. Vernooij, T. Huthwelker, H. Ade, D. Kilcoyne, T. Tyliszczak, R. H. Fink, and C. Quitmann, *Rev. Sci. Instrum.* **79**, 113704 (2008).
- S. Finizio, S. Wintz, B. Watts, and J. Raabe, *Microsc. Microanal.* **24**, 452 (2018).
- R. Nakajima, J. Stöhr, and Y. U. Idzerda, *Phys. Rev. B* **59**, 6421 (1999).
- U. Flechsig, C. Quitmann, J. Raabe, M. Böge, R. Fink, and H. Ade, *AIP Conf. Proc.* **879**, 505 (2007).
- D. Jiles, T. Chang, D. Hougen, and R. Ranjan, *J. Phys.* **49**, 1937 (1988).
- P. Talagala, P. S. Fodor, D. Haddad, R. Naik, L. E. Wenger, P. P. Vaishnava, and V. M. Naik, *Phys. Rev. B* **66**, 144426 (2002).
- See <http://feellgood.neel.cnrs.fr> for documentation on the FeellGood micro-magnetic simulator.
- S. Jamet, S. D. Col, N. Rougemaille, A. Wartelle, A. Locatelli, T. O. Menteş, B. S. Burgos, R. Afid, L. Cagnon, J. Bachmann, S. Bochmann, O. Fruchart, and J. C. Toussaint, *Phys. Rev. B* **92**, 144428 (2015).